Journal of Physics and Chemistry of Solids 216 (2026) 113756

Contents lists available at ScienceDirect

Journal of Physics and Chemistry of Solids

journal homepage: www.elsevier.com/locate/jpcs

Effects of Ni doping on the structural, vibrational, and magnetic properties and on the hydrogen evolution reaction in the $FeNbO_4$ compound

Diego S. Evaristo [a,*], Raí F. Jucá [b], Francisco G.S. Oliveira [a], Gilberto D. Saraiva [a], João M. Soares [c], Teresa M. Barreto [d,e], Pedro Tavares [d,e], Benilde F.O. Costa [f], José A. Paixão [f], Ana C. Silva [g], Nilson S. Ferreira [b], Marcelo A. Macedo [b], Antônio J.R. Castro [h]

[a] Faculdade de Educação, Ciências e Letras do Sertão Central, Universidade Estadual do Ceará, Quixadá, CE, 63902-098, Brazil
[b] Departamento de Física, Universidade Federal de Sergipe, 49100-000, São Cristóvão, SE, Brazil
[c] Departamento de Física, Universidade do Estado do Rio Grande do Norte, 59610-210, Mossoró, RN, Brazil
[d] UCIBIO – Applied Molecular Biosciences Unit, Department of Chemistry, NOVA School of Science and Technology, Universidade NOVA de Lisboa, 2829-516, Caparica, Portugal
[e] Associate Laboratory i4HB – Institute for Health and Bioeconomy, NOVA School of Science and Technology, Universidade NOVA de Lisboa, 2829-516, Caparica, Portugal
[f] University of Coimbra, CFisUC, Department of Physics, P-3004-516, Coimbra, Portugal
[g] Nova School of Science and Technology FCT-NOVA, New University of Lisbon, Campus da Caparica, P-2825, Caparica, Portugal
[h] Universidade Federal do Ceará, Campus Quixadá, 63902-580, Quixadá, Ceará, Brazil

ARTICLE INFO

Keywords:
Structural properties
Vibrational properties
Magnetic transition
Hydrogen evolution reaction

ABSTRACT

In this study, we conducted a comprehensive experimental investigation on nickel-doped iron niobate ceramics ($Fe_{1-x}Ni_xNbO_4$ with $x = 0.0 - 0.25$) crystallized in the monoclinic wolframite phase. The samples were characterized by X-ray diffraction (XRD), scanning electron microscopy (SEM), X-ray Photoelectron Spectroscopy (XPS), Raman spectroscopy, electron paramagnetic resonance (EPR), field-dependent ($M - H$) and temperature-dependent (M-T) magnetization, and measurements of the hydrogen evolution reaction (HER). XRD and Raman analyses revealed local structural distortions induced by the substitution of Fe^{3+} ions (3 d^5, $S = 5/2$) by Ni^{2+} ions (3 d^8, $S = 1$). Magnetic characterizations, including $M - H$ isotherms, M-T measurements, and EPR spectra, indicated the emergence of ferrimagnetic ordering, evidencing an antiferromagnetic (AFM) to ferrimagnetic (FiM) transition. The origin of ferrimagnetic ordering can be attributed to the increase in oxygen-mediated superexchange interactions between Fe and Ni ions (Ni^{2+}-O-Fe^{3+}) and the formation of oxygen vacancies. Electrochemical measurements demonstrated promising activity in the hydrogen evolution reaction (HER), with an overpotential of approximately 617 mV at a current density of 10 $mAcm^{-2}$ and a Tafel slope of 184 mV/decade for the composition $x = 0.20$. Furthermore, a negligible loss of overpotential was observed after 120 consecutive hours of hydrogen evolution. These results suggest that Ni-doped $FeNbO_4$ possesses considerable potential for applications in sustainable hydrogen production.

1. Introduction

The inherent need for sustainable energy sources has made the promotion of creative and environmentally friendly processes for the production of clean and renewable energy absolutely essential [1]. In this perspective, hydrogen sources stand out, attracting increasing attention due to their high calorific value, carbon-free properties, and environmentally friendly nature, without pollutant emissions [1]. Molecular hydrogen (H_2) can be produced by various methods, with water electrolysis being one of the most efficient. The electrolysis process involves two main reactions: the first is the hydrogen evolution reaction (HER), which occurs at the cathode, and the second is the oxygen evolution reaction (OER) at the anode, making it a promising method for large-scale hydrogen production [2]. The most commonly used catalysts

* Corresponding author.
E-mail address: daevaristo10@gmail.com (D.S. Evaristo).

https://doi.org/10.1016/j.jpcs.2026.113756
Received 22 December 2025; Received in revised form 24 March 2026; Accepted 10 April 2026
Available online 17 April 2026

are based on noble metals, such as platinum (Pt), palladium (Pd), and ruthenium (Ru). However, the high cost and limited availability represent a substantial barrier. This has led to the need to investigate the potential of other materials, especially transition metals, which are more economical and abundant in the Earth's crust [3]. Alloys [3], oxides [4], sulfides [5], and nitrides [6] of transition metals have been extensively studied for their activity in the hydrogen evolution reaction (HER). Compounds based on Fe and Nb have stood out due to their excellent electrochemical and catalytic properties [7–9]. Thus, the compound $FeNbO_4$ shows great promise for providing greater stability in the water electrolysis process.

$FeNbO_4$ is a polymorphic compound that crystallizes in three distinct crystalline phases depending on the annealing temperature [10]. The most stable, under ambient conditions, has monoclinic symmetry (m-$FeNbO_4$, space group *P2/c*) and is obtained at temperatures below 1085 °C [11]. Its crystal has ordered cations, where both Fe^{3+} and Nb^{5+} ions form octahedrons coordinated by six oxygen ions, forming almost one-dimensional zigzag-shaped chains of FeO_6 and NbO_6 [see Fig. 1(a and b)], along the (0, 0, 1) plane [11,12]. The crystal structure with orthorhombic symmetry (o-$FeNbO_4$) belonging to the space group Pbcn is obtained between 1085 and 1380 °C [13]. Unlike the m-$FeNbO_4$ phase, at temperatures above 1100 °C, the distribution of cations in this structure becomes completely disordered, where both Fe^{3+} ions and Nb^{5+} ions can occupy the same atomic sites [14]. Above 1380 °C it crystallizes in tetragonal phase (t-$FeNbO_4$, space group $P4_2/mnm$) [13,15]. All three phases exhibit *n*-type semiconducting behavior, with a relatively narrow bandgap ranging from 1.81 to 2.25 eV [16,17]. These properties make $FeNbO_4$ an attractive material for various applications, including sonocatalyst for wastewater treatment [18], effective catalyst for NO reduction and CO oxidation [19], green catalysts [7], photocatalysis [20,21], gas sensors [17], capacitors [22], lithium-ion batteries [23,24], as well as for anode material in solid oxide fuel cells [25].

The magnetic properties of these compounds are closely related to the distribution of cations throughout the structure and the degree of order/disorder depends on the specific synthesis conditions [26]. Oxygen-mediated superexchange interactions (Fe^{3+}-O-Fe^{3+}) are primarily responsible for the magnetic responses of these compounds. In particular, m-$FeNbO_4$ is isostructural to $FeWO_4$, where intra-chain interactions (short-range ordering, Fe^{3+}-O-Fe^{3+}) result in FM ordering, forming infinite FM sheets along the [1 0 0] [10]. Meanwhile, interchain interactions (long-range ordering, Fe^{3+}-O-Nb-O-Fe^{3+}) lead to an antiferromagnetic (AFM) arrangement in the structure, with Néel temperature of approximately 38.5 K [14,27]. However, recent studies have shown that doping $FeNbO_4$ with transition metal ions such as Cu^{2+} can induce a transition from AFM to FiM behavior when the doping level exceeds $x = 0.05$ [27]. The origin of the transition was associated with the breaking of magnetic symmetry, attributed to the interactions between the Fe^{3+} (3 d^5, $S = 5/2$) and Cu^{2+} (3 d^9, $S = 1/2$) ions, mediated by oxygen (Cu^{2+}-O-Fe^{3+}), and contribution of defects, such as oxygen vacancies. These results open precedents for broader and more comprehensive investigations into potential dopants capable of causing significant changes in the chemical and physical properties of the $FeNbO_4$ compound. This may include theoretical and/or experimental approaches that could contribute to elucidating the role of defects on the structural properties of the $FeNbO_4$.

In this work, we evaluated the influence of the replacement of Fe^{3+} ions by Ni^{2+} ions (3 d^8, $S = 1$) on the structural, vibrational, and magnetic properties of the ordered $FeNbO_4$ structure. Our results show that replacing Fe^{3+} with Ni^{2+} significantly changes structural properties. Ni^{2+} insertion into the Fe^{3+} site causes significant local changes, such as variations in bond length and bond angle, which directly reflect an increase in the total unit cell volume. Furthermore, it promotes an increase in cationic disorder, resulting in changes in magnetic properties. This increase in disorder is confirmed by Raman spectroscopy. The increased Ni^{2+} insertion (for $x > 0.05$) causes a global magnetic order transition from an AFM to a FiM state, which can be associated with increased local superexchange interactions between Ni^{2+}-O-Fe^{3+} ions and the contribution of defects such as oxygen vacancies. In addition, we evaluated the electrochemical properties. Our results suggest that Ni-doped $FeNbO_4$ possesses considerable potential for applications in sustainable hydrogen production.

2. Experimental details

All samples were prepared by the conventional solid-state reaction method, having as starting materials with P.A grade: iron oxide III (Fe_2O_3 – Sigma, 96%), nickel oxide (NiO – Sigma, 99%) and niobium pentoxide (Nb_2O_5 – Sigma, 99%). The reagents were calculated in the stoichiometrically appropriate ratio ($Fe_{1-x}Ni_xNbO_4$, x = 0.0 - 0.25), mixed and subsequently dried in a muffle furnace at 600 °C/2h, followed by grinding at 200 rpm and sintering at 1200 °C/12h in ambient atmosphere. The structural characterization was analyzed by the X-ray diffraction (Rigaku) using Cu-Kα radiation (λ = 1.54 Å) in the range of 20-70°, the step of 0.01° and counting time by step of 2s. The crystal

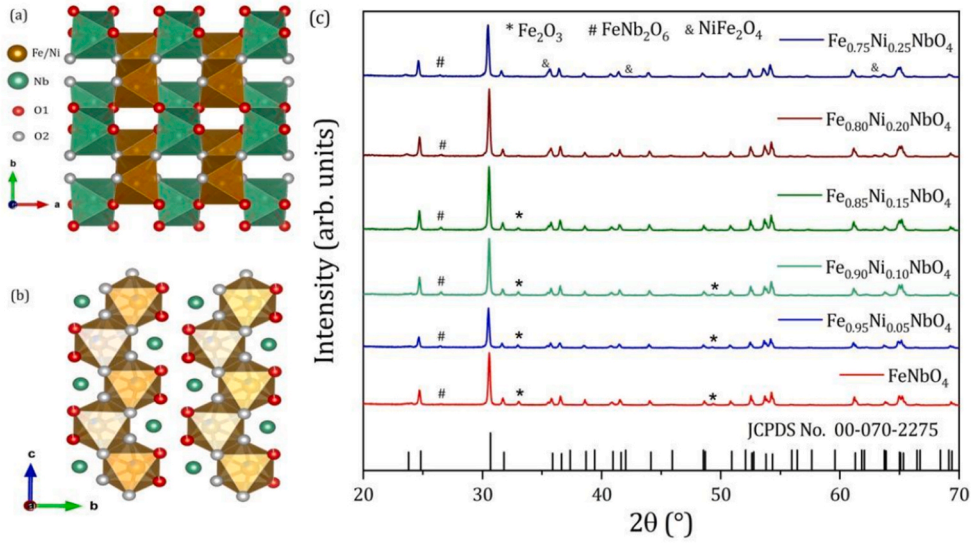

Fig. 1. (a). Illustrative scheme of the $Fe_{1-x}Ni_xNbO_4$ crystal structure. (b) View along the b-axis showing the zig-zag distribution of cations in the lattice. (c) XRD profile for the $Fe_{1-x}Ni_xNbO_4$ samples (x = 0.00–0.25).

structures lattice parameters were refined using the Rietveld method with the GSAS Software [28]. The vibrational properties of the samples were investigated using a Raman micro-spectrometer (Horiba LabRam HR Evolution), equipped with a Synapse CCD detector, a high-stability BXFM open-space confocal microscope, grating of 600 g/mm, and an excitation source with 532 nm. Raman spectra were recorded for the different samples over a wavenumber range of 100–900 cm^{-1}. Morphological analyses were performed using a high-resolution scanning electron microscope (SEM) Vega3 SBH model from TESCAN, equipped with an energy-dispersive spectrometer (EDS) (Bruker Xflash 410 M). The energy electron acceleration voltage was set to 20 kV. XPS measurements were performed using a VSW XPS system equipped with a Class 100 energy analyzer, integrated into a multi-technique surface analysis setup. The survey spectra were recorded in fixed transmission mode with a pass energy of 44 eV (FAT 44), employing a non-monochromatic Mg Kα radiation source (hν = 1253.6 eV). The binding energy scale was calibrated using the Ag 3d5/2 (368.22 eV) and Au 4f7/2 (83.96 eV) core levels. The O-1*s*, Nb-3*d*, Fe-2*p*, and Ni-2*p* core-level spectra were fitted using CasaXPS software. Shirley background subtraction was applied, and Gaussian–Lorentzian functions GL (30) were used as the fitting model for all spectra. The magnetization (*M*) versus applied magnetic field (*H*) plots were obtained at room temperature using vibrating sample magnetometer (VSM, homemade) calibrated through a standard reference (powder high purity nickel), supplied with the instrument. These data have been analyzed to obtain the saturation magnetization (M_s) and coercive field (H_c) for ($Fe_{1-x}Ni_xNbO_4$, $x = 0.0$ - 0.25) sample in powder form. The thermomagnetic *M* (*T*) curves were measured in a Quantum Design Dynacool PPMS equipped with a 9 T superconducting magnet and using the VSM option. Data were collected on heating under an applied field of 1 kOe, after zero field cooling (ZFC), followed by a measurement on cooling under the same value of the applied field. The cooling/heating rates were identical (1 K/min) within the 5 – 300 K spanned temperature range. EPR spectra of powder samples contained in 10 μL glass capillary (Duran Ringcaps, Hirschmann, Germany) were acquired using a MiniScope MS 400 X-band EPR spectrometer (Magnettech Germany) equipped with a Suprasil Nitrogen Dewar (SP Wilmad-LabGlass, USA) for measurements at 77 K. The EPR data at room temperature were acquired with four scans accumulations of 60 s for each sample, using the following parameters: modulation amplitude, 0.5 or 0.7 mT; attenuation, 6 to 24 dB; gain, 100 or 200; MW frequency, 9.46 GHz. At 77 K the data acquisition was acquired with: four scans of 60 s were accumulated for each sample using the following parameters: modulation amplitude, 0.2 to 0.7 mT; attenuation, 6 to 24 dB; gain, 50; MW frequency, 9.42 GHz. All details of the experimental procedures used for the electrochemical tests can be found in Ref. [2].

3. Results and discussion

3.1. Structural study

The $Fe_{1-x}Ni_xNbO_4$ ($x = 0.00 – 0.25$) samples were characterized at room temperature using powder X-ray diffraction (XRD). The corresponding diffraction patterns are shown in Fig. 1(c). The XRD patterns reveal that all samples present a monoclinic phase, belonging to the space group *P*2/*c* (No. 13), indexed through the ICDD pattern (00-070-2275), where the reflection planes (1 1 0) and (2 1 -1) observed at 24.6° and 45.8°, respectively, are characteristic of the structure [14].

Furthermore, it is also possible to observe the presence of small impurity phases that were indexed with the following phases α-Fe_2O_3 (ICSD-082903) in the rhombohedral phase (*R*-3*c*), $FeNb_2O_6$ (ICSD-047187) in the tetragonal phase ($P\text{-}42_1m$) and $NiFe_2O_4$ (ICSD-073676) in the cubic phase (*Fd*-3*m*), respectively. The secondary phases α-Fe_2O_3, $FeNb_2O_6$ and $NiFe_2O_4$, resulting from segregation regions and incomplete reaction of reactants, were marked as *, # and & as shown in Fig. 1 (c).

The Rietveld refinement XRD patterns for the samples with $x = 0.00$ and 0.25 are shown in Fig. 2(a) and (b), respectively. The refinement of the X-ray diffraction of the remaining samples is described in the Supplement Material (Fig. S1). The values obtained for the refinement quality factors such as χ^2, R_{wp} and R_p reflect that the refined results are reliable. The results obtained for all samples can be seen in Table 1. Furthermore, the majority phase of m-$FeNbO_4$ was quantified with 96.05%, 95.00%, 95.19%, 96.94%, 98.00% and 95.62% for x = 0.0, 0.05, 0.10, 0.15, 0.20 and 0.25 respectively. The incorporation of Ni^{2+} ions promotes some significant changes in the structural parameters (see Table 1), such as: (i) increase in bond length (*b* and *c*), angle β and cell volume [see Fig. 2(d)]; (ii) local changes in the FeO_6 and NbO_6 octahedral sites [see Fig. 2(c)] through bond length and angle; (iii) reduction in the Nb-O bond length, while Fe-O increased as a function of substitution, which is expected due to the small difference in the ionic radius of the substituent ($r_{Fe^{3+}} = 0.064\,nm$; $r_{Ni^{2+}} = 0.069\,nm$) indicating structural stability. Furthermore, a clear structural anisotropy is observed in the variation of the lattice parameters: while the *b* and *c* axes show continuous growth, the *a* parameter remains statistically invariant. This anisotropic expansion can be attributed to the structural rigidity of the [MO_6] octahedral chains along the [1 0 0] direction, where edge sharing imposes a geometric constraint that minimizes compressibility and thermal/chemical expansion in this axis. Conversely, expansion in *c* is favored by the greater flexibility of vertex connections between the chains, while the increase in *b* reflects the relaxation of interlayer electrostatic forces resulting from the lower cationic charge of Ni^{2+}. Thus, the lattice accommodates steric (or Van der Waals) strain and possible oxygen vacancies through angular rearrangement (octahedral distortions) and bond elongation in the directions of least crystallographic hindrance.

3.2. Raman spectroscopy

According to the analysis based on the irreducible representations of the factor group (C_{2h}), the crystal symmetry inherent to $FeNbO_4$ implies that the 3 N degrees of freedom arising from the 12 atoms in the primitive cell are distributed among 36 vibrational modes, denoted as:

$$\Gamma_{\text{vibração}} = 8A_g \oplus 10B_g \oplus 8A_u \oplus 10B_u \quad (1)$$

Within this set of 36 vibrational modes, 33 belong to optical modes (k = 0), yielding $\boldsymbol{\Gamma}_{\text{optical}} = 8A_g \oplus 10B_g \oplus 7A_u \oplus 8B_u$, while the remaining 3 correspond to acoustic modes, expressed as $\boldsymbol{\Gamma}_{\text{acoustic}} = A_u \oplus 2B_u$. All of these modes exhibit even (g) vibrations, making them Raman-active (18), while the odd (u) vibrations are declared to be IR-active (15) [27,29,30]. After decomposing the room-temperature Raman spectrum using Lorentzian functions, we identified 15 distinct vibrational bands located at 133, 146, 172, 206, 222, 271, 300, 318, 359, 389, 412, 463, 494, 594, and 816 cm^{-1}. These vibrational modes correspond harmoniously to the monoclinic phase $FeNbO_4$, as illustrated in Fig. 3(a) [27, 29–32]. The position of each vibration mode is briefly summarized in Table 2.

The analysis of the Raman modes as a function of the Ni insertion distinctly revealed the persistence of a stable crystal structure without any evidence of symmetry changes, as illustrated in Fig. 3(a). The deconvolution of the Raman spectra bands, fitted with a Lorentzian function, is shown for the $x = 0$ sample in Fig. 3(b). The deconvoluted Raman bands for the remaining $Fe_{1-x}Ni_xNbO_4$ ($0.05 \leq x \leq 0.25$) samples are presented in Fig. S2. The corresponding Raman shifts values obtained from the spectral deconvolution are summarized in Table 2. The introduction of Ni^{2+} ions induces localized atomic perturbations at each lattice sites, which manifest as an increase in frequencies and the full width at half maximum (FWHM), Fig. 3(c). For example, the Raman shift to the Ag symmetric stretching mode is observed at 816 cm^{-1} for $FeNbO_4$, while for $Fe_{0.75}Ni_{0.25}NbO_4$, it is centered at 826 cm^{-1}, representing a $\Delta\tilde{\upsilon}$ of 10 cm^{-1}. Similar results were observed for the Fe_{1-}

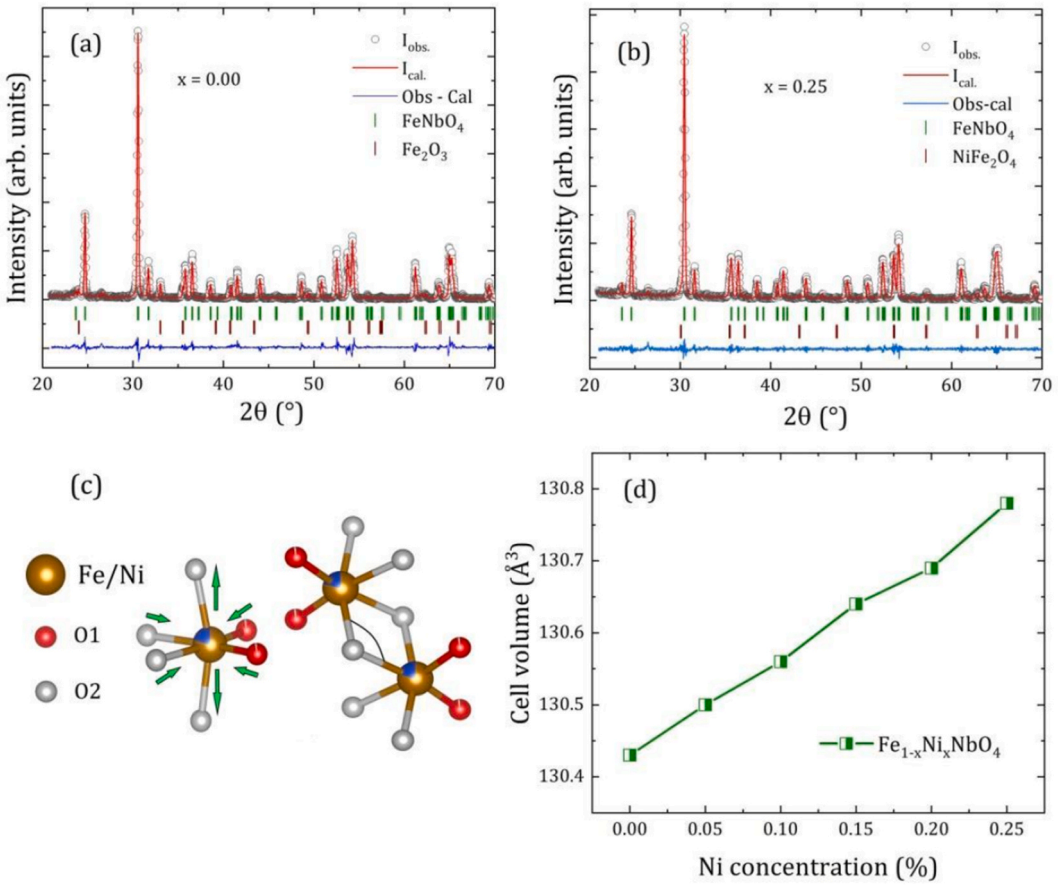

Fig. 2. Rietveld refined XRD profile for the $Fe_{1-x}Ni_xNbO_4$ samples for (a) $x = 0$ and (b) $x = 0.25$; (c) schematic illustration of the unit cell for $x = 0.25$ and (d) evolution of unit cell volume as a function of Ni-doping.

Table 1
Lattice parameters (a, b, c), angles ($\alpha = \gamma$, β), unit Cell Volume (V), Bond length, Angles, weighted profile factor (R_{wp}), profile factor (R_p), and chi (χ^2), estimated from the XRD pattern Rietveld refinement for $Fe_{1-x}Ni_xNbO_4$ samples ($x = 0.00$–0.25).

	Samples	0.00	0.05	0.10	0.15	0.20	0.25
Parameters	**a (Å)**	4.649(9)	4.647(3)	4.647(8)	4.648(9)	4.648(9)	4.649(4)
	b(Å)	5.616(7)	5.616(2)	5.618(8)	5.619(7)	5.620(6)	5.624(2)
	c(Å)	4.996(8)	4.997(0)	4.999(2)	5.000(5)	5.001(6)	5.004(3)
	α(°)	90.000	90.000	90.000	90.000	90.000	90.000
	β(°)	90.063(3)	90.050(5)	90.033(7)	90.049(6)	90.081(6)	90.079(8)
	γ(°)	90.000	90.000	90.000	90.000	90.000	90.000
	V(Å^3)	130.43	130.50	130.56	130.64	130.69	130.78
Length	**Fe-O1(Å)**	1.882(2)	1.946(0)	1.821(5)	1.919(8)	1.942(4)	1.932(8)
	Fe-O2(Å)	2.011(7)	2.026(7)	2.004(4)	1.968(8)	2.022(5)	2.004(2)
	Fe-O2(Å)	2.061(5)	2.183(1)	2.118(3)	2.149(9)	2.167(0)	2.156(0)
	Nb-O1(Å)	2.195(1)	2.114(3)	2.216(3)	2.158(5)	2.166(6)	2.128(9)
	Nb-O1(Å)	1.962(0)	1.955(9)	1.998(6)	1.957(9)	1.930(5)	1.950(9)
	Nb-O2(Å)	1.970(7)	1.878(3)	1.969(0)	1.949(7)	1.891(2)	1.922(6)
Angles	**Cu/Fe-O2-Fe(°)**	103.41	98.86	102.02	101.19	98.92	100.52
	Fe-O2-Nb(°)	129.73	127.62	126.98	124.98	127.25	127.46
Quality factors	**χ^2**	1.65	1.40	1.88	2.10	1.72	1.50
	R_{wp}(%)	15.8	16.0	16.2	14.8	14.6	14.5
	R_p(%)	5.5	7.6	7.4	6.8	5.1	6.0

$_x$Cu$_x$NbO$_4$ structure [27], and $Fe_{1-x}Co_xNbO_4$ structures [2]. The observed Raman shift, along with the increase in the FWHM, provided strong evidence that the incorporation of Ni^{2+} promotes cationic disorder within the monoclinic structure [27,33]. The substitution of Fe^{3+} by Ni^{2+} ions in the ordered lattice increases the cationic disorder, directly influencing the magnetic ordering [27]. Therefore, the persistence of the vibrational signature across all doping levels supports the XRD finding that the crystal structure remains unchanged, although local distortions intensify. These results confirm that Raman spectroscopy is a sensitive technique for detecting short-range structural perturbations that are not always resolved by XRD alone, especially in lightly doped systems.

3.3. Morphological and compositional analysis

The particle size and chemical composition of the samples were

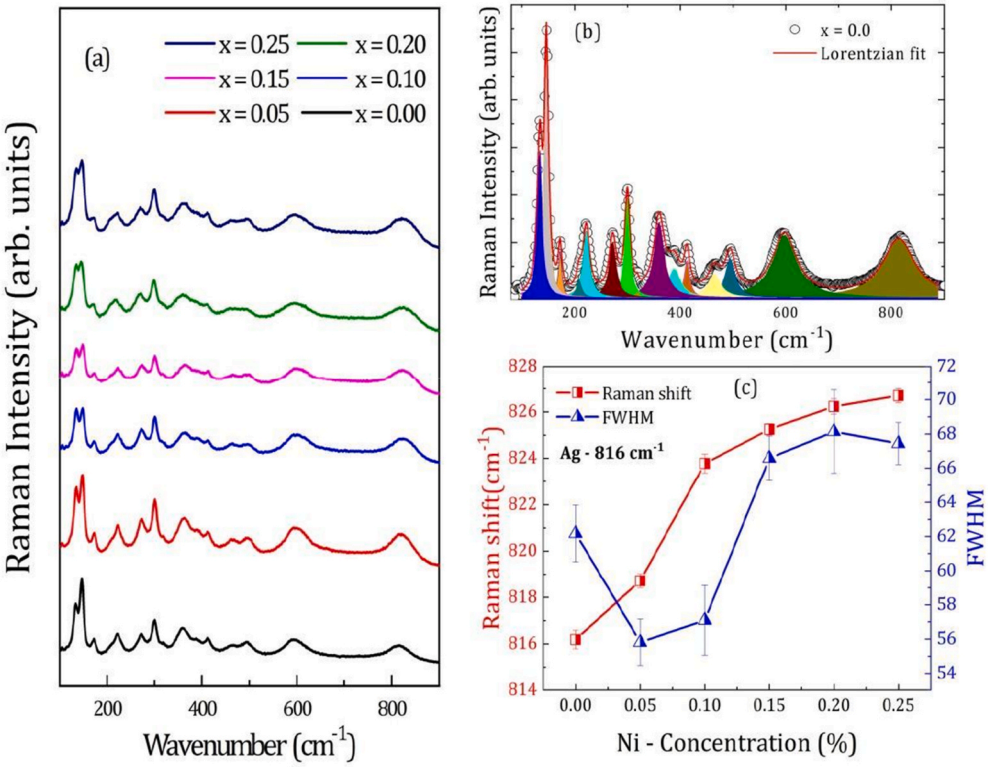

Fig. 3. (a) Spectra Raman of the $Fe_{1-x}Ni_xNbO_4$ ($x = 0.00$-0.25) samples; (b) deconvolution profile of the Raman modes for $x = 0.0$; and (c) displacement and FWHM as a function of Ni^{2+} concentration, showing the influence of Ni^{2+} on the vibration modes 816 cm^{-1} (A_g).

Table 2
Active vibration mode in the Raman spectrum for $Fe_{1-x}Ni_xNbO_4$ (x = 0.0 – 0.25).

ω_{obs} (cm^{-1})						Sym.
0.00	**0.05**	**0.10**	**0.15**	**0.20**	**0.25**	
133.94	134.05	135.71	135.56	135.55	135.48	A_g
146.23	147.51	147.89	148.30	144.99	146.46	B_g
172.05	172.76	172.90	172.73	171.37	172.11	B_g
206.78	-	-	-	-	206.76	A_g
222.00	221.90	221.69	222.58	216.98	221.46	B_g
271.50	277.03	272.86	273.65	270.01	270.17	A_g
299.86	300.42	300.17	300.46	298.75	299.11	B_g
318.92	318.89		317.73		318.88	A_g
359.63	362.15	363.05	364.25	362.77	361.76	A_g
389.38	390.59	390	391.38	387.48	389.68	B_g
412.15	412.72	412.13	412.88	411.13	412.62	B_g
463.36	463.91	463.90	465.85	462.26	461.05	B_g
494.50	497.13	497.19	496.46	489.07	495.72	A_g
594.74	598.53	598.43	599.50	598.92	594.93	B_g
816.19	818.72	823.78	825.25	826.23	826.70	A_g

examined by scanning electron microscopy (SEM/EDS) images, as are shown in Fig. 4 and Fig. S3. The magnified surface images of the $FeNbO_4$ [Fig. 4(a)] and $Fe_{0.75}Ni_{0.25}NbO_4$ [Fig. 4(b)] samples reveal a non-uniform distribution of particle sizes across the samples. The particle size is in the microscale range (microparticles), ranging from 0.8 μm to 15 μm, with an average diameter of ~ 6-7 μm, respectively. The particle size distribution, along with the corresponding fitting curve, is shown in insert Fig. 4. The EDS spectra together with the data table (including atomic and mass percentages for each element) are shown in Fig. S4. The results indicate stoichiometric proximity for the ionic ratio of Fe and Nb, with respective average values of 0.93:1 (Fe:Nb) for the sample $x = 0.0$. However, for the sample with the highest doping concentration ($x = 0.25$), there is a significant difference in the nominal stoichiometric ratio obtained for Ni. The average values obtained were 0.75/0.11:1 for Fe/Ni: Nb, respectively. The loss of Ni may have occurred during the sample preparation procedures, during the milling process, or even due to diffusion into the alumina crucible at high temperature.

3.4. X-ray Photoelectron Spectroscopy (XPS)

The XPS spectra of $Fe_{0.75}Ni_{0.25}NbO_4$ are presented in Fig. 5, while the spectra of the undoped $FeNbO_4$ sample are shown in the supplementary material (Fig. S5). The Fe-2*p* spectrum (Fig. 5(a)) exhibits the characteristic Fe-2$p_{3/2}$ multiplet structure associated with Fe^{3+} species. The main contributions are centered at approximately 709.4, 710.4, 711.6 and 712.9 eV, which are typical binding energies for Fe^{3+} in Fe_2O_3 like environments [34,35]. In addition, a small contribution centered around 714.7 eV suggests the possible presence of a minor FeOOH surface component, although its contribution is relatively small [36]. The Nb-3*d* spectrum (Fig. 5(b)) displays the typical spin–orbit doublet corresponding to the Nb-3$d_{5/2}$ and Nb-3$d_{3/2}$ components, with a spin–orbit splitting of about 2.72 eV. The XPS results indicate that niobium is predominantly present in the Nb^{5+} oxidation state, consistent with the Nb_2O_5 chemical environment commonly observed in niobate compounds [18,37]. These results suggest that the high-valence state of niobium is preserved after Ni substitution.

The Ni-2*p* spectrum (Fig. 5(c)) confirms the successful incorporation of nickel into the structure. The Ni-2$p_{3/2}$ region shows contributions characteristic of Ni^{2+} species, typically associated with $Ni(OH)_2$ and NiOOH surface phases [38,39]. The contribution at lower binding energy around 854.8 eV is attributed to overlapping components related to different Ni oxidation states, partially superimposed with multiplet features centered near 855.3 eV. The most intense contribution, centered at approximately 857.2 eV, is mainly attributed to Ni^{2+} species associated with $Ni(OH)_2$ and β-NiOOH [38,39]. This contribution represents about 73.3% of the total Ni-2*p* signal, indicating that Ni^{2+} is the dominant oxidation state in the doped sample. Finally, the O 1s spectrum (Fig. 5(d)) reveals two main components. The peak located at approximately 529.6 eV corresponds to lattice oxygen (O_L) associated

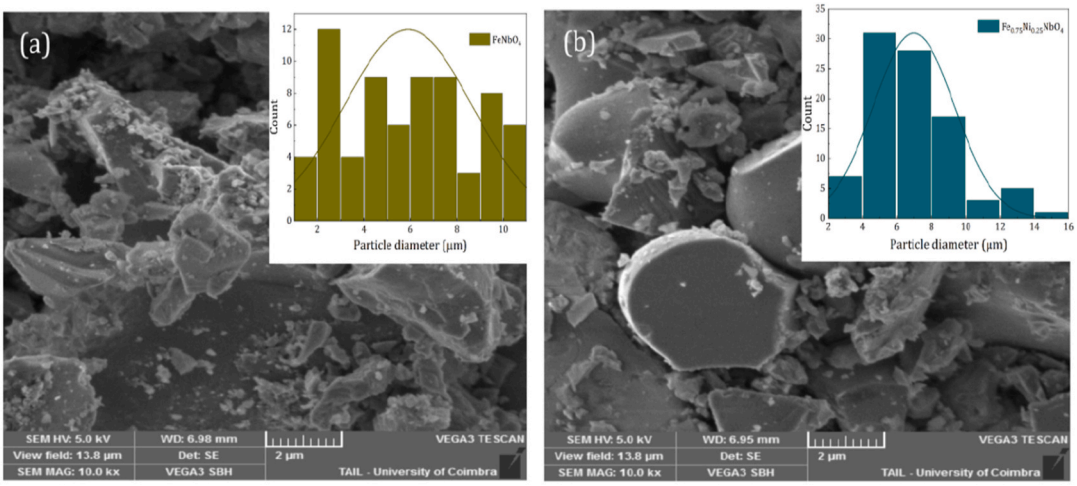

Fig. 4. SEM images and particle size distribution: (a) $FeNbO_4$, (b) $Fe_{0.75}Ni_{0.25}NbO_4$.

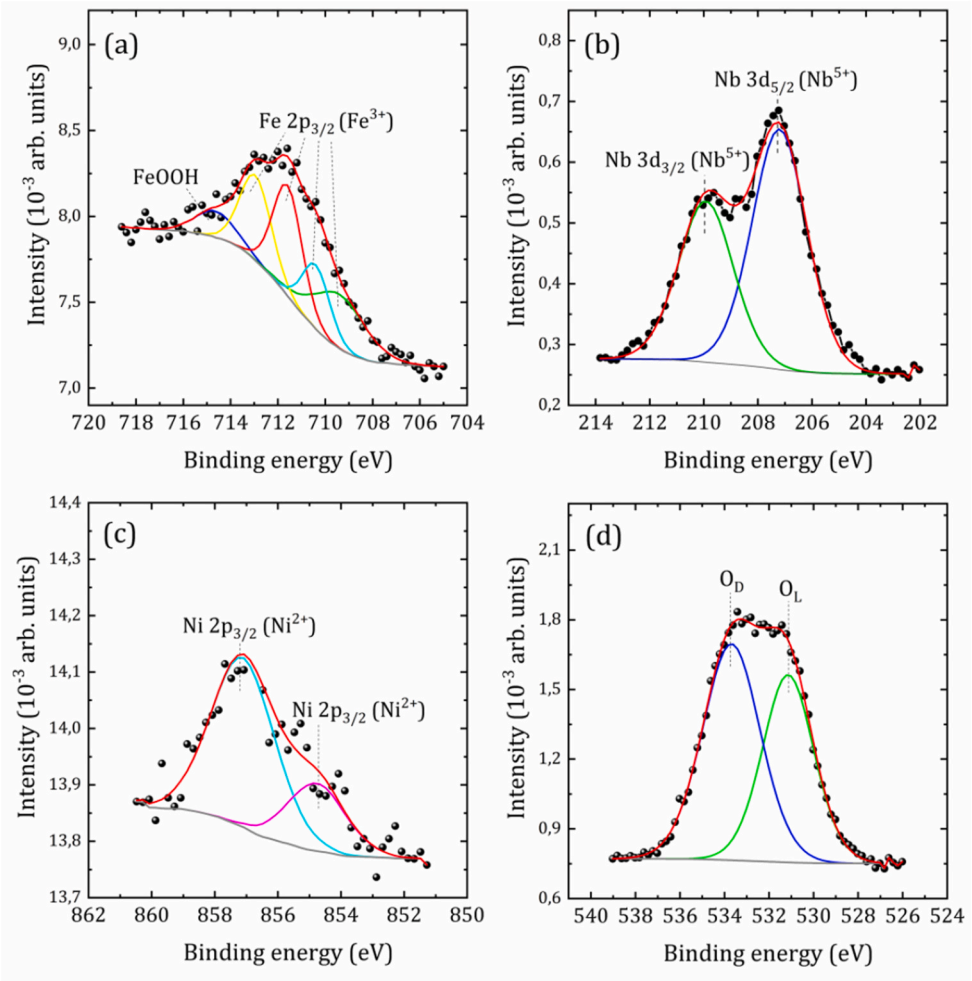

Fig. 5. High-resolution XPS spectra for the (a) Fe-2*p*, (b) Nb-3*d*, (c) Ni-2*p* and (d) O-1*s* energy levels of the $Fe_{0.75}Ni_{0.25}NbO_4$ sample.

with the metal–oxygen framework [20]. The second contribution, centered near 531.2 eV, is attributed to defective (O_D), which may arise from oxygen vacancies or structural disorder [20]. The presence of this higher binding energy component suggests the existence of surface defects or oxygen-deficient environments, which may influence the catalytic properties of the material.

3.5. Magnetics properties

The magnetic behavior as a function of doping was obtained through field-dependent magnetization (*M vs. H*) measurements at room temperature, are shown in Fig. 6(a). For low Ni concentrations ($x = 0.00$ and 0.05), a gradual and linear increase in magnetization is observed with

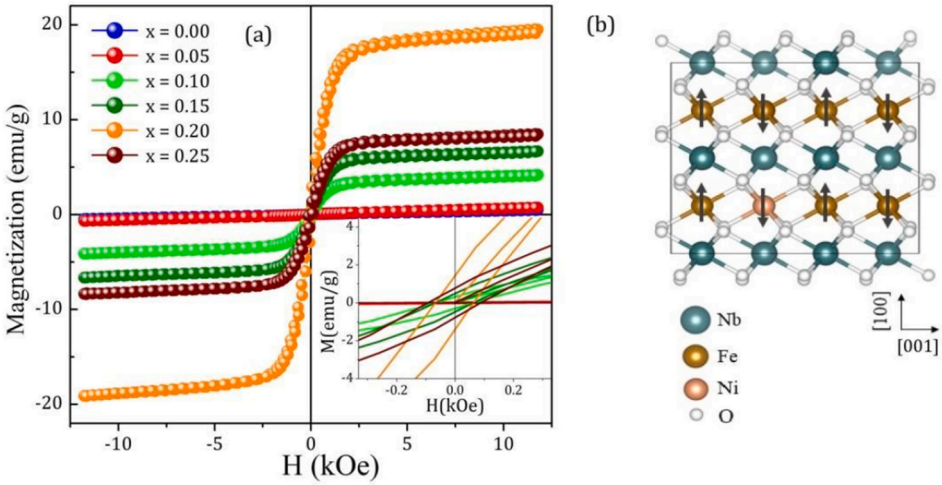

Fig. 6. (a) $M - H$ curves for $Fe_{1-x}Ni_xNbO_4$ (x = 0.0–0.25) under applied magnetic field; (b) Schematic illustration of a ferrimagnetic (FiM) ordering configuration observed in the $Fe_{1-x}Ni_xNbO_4$ material.

increasing applied magnetic field, as shown Fig. 6(a) and in detail in Fig. S6. At low field values, a small deviation from linearity can be observed, which may be associated with contributions from magnetic impurities, α-Fe_2O_3. However, for concentration above x = 0.05, a noticeable change in the magnetization behavior can be observed. The M versus H curve exhibits a significant increase in the magnetization, an S-shaped curve, and the emergence of a coercive field (H_c) and remanent magnetization (M_r). These features indicate a magnetic phase transition process from AFM to FiM as a function of Ni insertion. Similar magnetic order transitions were recently reported for $Fe_{1-x}Cu_xNbO_4$ [27] and in systems such as $(Fe_{1-x}Mn_x)_2Mo_3O_8$ ($x > 0.25$) [40] and $(Mn_{1-x}Co_x)_2Mo_3O_8$ ($0 \leq x \leq 1$) [41].

The inset of Fig. 6(a) shows the dependence of H_c and M_r on the Ni concentration in the low-field region. All data extracted from the magnetization curves can be seen in Table 3. In Fig. 6(b) we can observe an illustrative representation of a FiM ordering configuration observed in the material. The AFM transition to FiM can be associated with a breaking of magnetic symmetry due to the difference in magnetic moment between the Fe^{3+} ($\mu_{eff} = 5.92\ \mu_B$) and Ni^{2+} ($\mu_{eff} = 2.83\ \mu_B$) ions, that is, the substitution of Fe^{3+} ions (S = 5/2) by Ni^{2+} ions (S = 1) modifies the short-range exchange interactions, altering the local magnetic ordering. Thus, the increase in Ni^{2+} insertion significantly increases the exchange interactions between Ni^{2+} and Fe^{3+} ions (Ni^{2+}-O-Fe^{3+}), which contribute to the increased magnetization observed in the M *vs* H curves, Fig. 6(a). Furthermore, contribution from defects such as oxygen vacancies, which can alter the exchange path, can also be responsible for the global FiM order observed in the $Fe_{1-x}Ni_xNbO_4$ structure, for $x > 0.05$. For x = 0.25, a significant reduction in magnetization is observed. This can be attributed to the stoichiometric loss of Ni (as shown in the EDS measurement, Fig. S3), which considerably decreases the Fe/Ni interactions and, as a result, the magnetic response.

The temperature (T)-dependent magnetization (M) was evaluated to understand the magnetic transition in the $Fe_{1-x}Ni_xNbO_4$ compound. The measurements were performed for the samples x = 0.0 and 0.25. The M *vs* T curves in the field cooling (FC) and zero-field cooling (ZFC) modes, for x = 0.0, are presented in Fig. 7(a) with a magnetic field (H) of 1 kOe. Only a small difference is found between the FC and ZFC curves in the low temperature range. Furthermore, significant magnetic transition signals can be observed at two temperatures in both curves (FC and ZFC). The susceptibility drift as a function of temperature (dχ/dT), shown in Fig. 7(b), evidences two transitions at T_{N1} = 254 K and T_{N2} = 44 K, respectively. T_{N1} is associated with the AFM ordering transition of α-Fe_2O_3, defined as the Morin transition [42]. T_{N2} is associated with the transition from the PM state to the AFM ordered state of the $FeNbO_4$ compound. The T_{N2} value is in good agreement with the values obtained in the literature [14,27]. Notably, the $1/\chi$(T) curves [Fig. 7(c)] in the PM region obey the Curie-Weiss law, $\chi(T) = C/(T - \theta_{cw})$, where C and θ_{cw} represent the Curie constant and the Curie paramagnetic temperature, respectively, and $C = N(\mu_B\ \mu_{eff})^2 / 3k_B$ (where μ_{eff} denotes the effective magnetic moment) [43]. Linear fits from 50 K to 220 K produced a negative θ_{cw} value of −155 K for $FeNbO_4$, which confirms that the predominant magnetic interaction is of an AFM nature. The corresponding value of μ_{eff} was determined to be 6.56 μ_B, which is larger than that when considering only the theoretical magnetic moment of the Fe^{3+} ions (5.92 μ_B). However, this increase can be attributed to the magnetic contributions of impurity phases present in the sample. The frustration factor is calculated as $f = |\theta_{CW}|/T_N = 3.52$.

The FC and ZFC curves for the x = 0.25 sample are shown in Fig. 7 (d). Initially, the FC and ZFC curves exhibit similar behavior, with a gradual increase in magnetization as the temperature decreases up to approximately 140 K. Below 140 K, the ZFC measurement exhibits distinct behavior from FC, with a reduction in magnetization as the temperature decreases. Surprisingly, below 50 K, both curves exhibit characteristics of AFM ordering. The inverse susceptibility curve shown in the inset of Fig. 7(d) highlights this AFM ordering region. These results provide evidence of a FiM/AFM magnetic transition due to temperature in the x = 0.25 sample. Similar behavior was observed in the $Fe_{0.75}Cu_{0.25}NbO_4$ structure [44]. However, further studies are needed to elucidate this behavior. Furthermore, the magnetization curves exhibit a much higher magnetic response than that of the x = 0.0 sample (more than 25 times higher). This result confirms the magnetic transition from AFM to FiM by doping effect discussed in the M *vs* H curves, Fig. 6(a). The insertion of Ni in the $FeNbO_4$ structure influences the local magnetic interactions (Ni^{2+}-O-Fe^{3+}), changing the global ordering state of the $Fe_{0.75}Ni_{0.25}NbO_4$ structure, which now presents a new ordering state, FiM.

Table 3
Magnetic parameters: maximum magnetization (M_{max}), initial saturation magnetization (M_0), coercive field (H_c) and remanent magnetization (M_r).

Samples	M_{max} (emu/g)	M_0 (emu/g)	H_c (kOe)	M_r (emu/g)
0.00	0.4914	0.0929	0.2579	0.0224
0.05	0.7407	0.1399	0.2244	0.0358
0.10	4.1688	3.3672	0.0621	0.3130
0.15	6.6658	5.8132	0.0627	0.4885
0.20	19.5113	17.2446	0.0632	1.4555
0.25	8.4785	7.5042	0.0876	0.7772

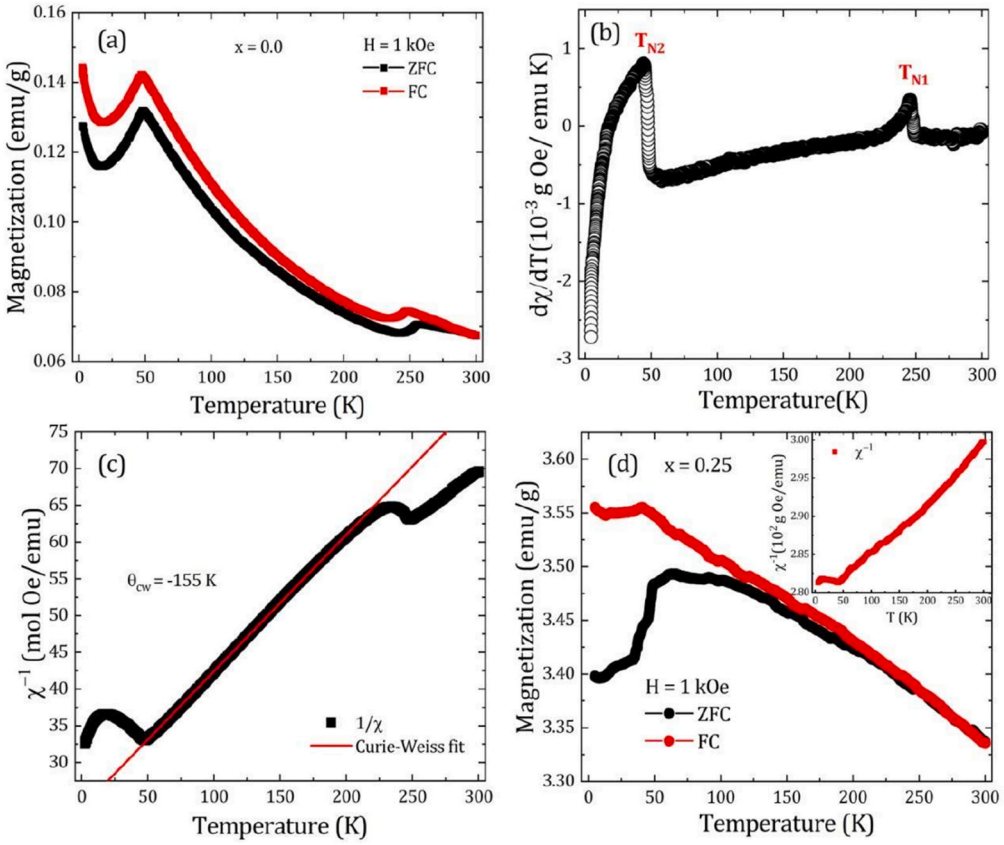

Fig. 7. (a) Temperature-dependent magnetization curves (FC and ZFC) with an applied field of 1 kOe for $x = 0.0$; (b) derivative of the magnetic susceptibility (dχ/dT) as a function of temperature for $x = 0.0$, showing two transition temperatures, T_{N1} and T_{N2}, for $x = 0.0$; (c) Inverse susceptibility curve as a function of temperature (χ^{-1}*vs T*) fitted by the Curie–Weiss law; (d) Temperature-dependent magnetization curves (FC and ZFC) with an applied field of 1 kOe for $x = 0.25$. The inset shows the inverse susceptibility curve (χ^{-1}*vs T*).

3.6. Electron paramagnetic resonance

The EPR spectra measured at room temperature (300 K) and at low temperature (77 K) for the $Fe_{1-x}Ni_xNbO_4$ samples ($x = 0.00$ and 0.25) are shown in Fig. 8. All EPR spectra are shown in Fig. S7. The resonance line width ΔH_{pp} is defined as the peak-to-peak distance, and the effective *g*-factor is experimentally defined as $h\nu/\beta H_r$, where ν is the microwave frequency, H_r is the magnetic field where the photon energy is equal to the separation of the electronic energy level, *h* is Planck's constant, and β is the Bohr magneton [45].

The EPR spectrum of the sample with the highest Ni concentration ($x = 0.25$), Fig. 8(a), shows a resonance spectrum with a sharp reduction of ΔH_{pp}, compared to the $FeNbO_4$ sample, i.e., a reduction of more than a factor of four, with respective values of $\Delta H_{pp} = 52.03$ mT and $g = 2.27$. Furthermore, as the temperature decreases to 77 K, the ΔH_{pp} signal broadens, while H_r shows a small decrease. The *g* values found, between 2.28 and 2.31, are in good agreement with that reported for the super-exchange coupled pair between Fe^{3+} and Ni^{2+} ions (Fe^{3+}-O-Ni^{2+}) [45,46]. This behavior can be attributed to the g values approach for the range of values (2.2 - 2.3) that normally define the spectrum for Ni^{2+} ions, while the Fe^{3+} usually exhibits *g*-values closer to 2.0 [45].

The spectrum of the $FeNbO_4$ sample at 300 K [Fig. 8(b)] shows a relatively broad signal with a linewidth of $\Delta H_{pp} = 215.84$ mT and a calculated *g* value of approximately 2.26. As the temperature decreases to 77 K, the value of ΔH_{pp} increases while H_r decreases. There are a few possible explanations for this behavior: The first possibility is that the sudden change in H_{res} and the broadening in ΔH_{pp} as the temperature is reduced can be understood as a manifestation of the existence of short-range AFM correlations in the PM phase [47]. This temperature dependence of our EPR data can be understood in terms of a universal behavior for the spin dynamics seen in many classes of materials, which reveals short-range interaction between Fe^{3+} and Fe^{3+} ions just above the AFM order [47]. However, this fact would reveal a magnetically frustrated character of this compound because strong AFM correlations exist well above T_N, which is something remote [47]. Another more solid explanation is associated with the formation of iron clusters that give rise to super exchange-type interactions between Fe^{3+} ions and contribute to paramagnetic resonance [47]. Furthermore, in our EPR data, magnetic impurities may also have contributed to this shift, since a small resonance signal is also observed at about $g = 4.24$, which can be attributed to the Fe_2O_3 impurity present in the sample, and can be associated with the Fe^{3+}-O-Fe^{3+} spin pair interactions, respectively. This suggests that the $FeNbO_4$ sample may have a α-Fe_2O_3 impurity at an EPR detectable level of >3 mol (%) [45], as shown in the XRD profile, Fig. 1 (c). The *g* value of 2.26 found for the oxygen-mediated superexchange interactions between Fe^{3+} ions (Fe^{3+}-O-Fe^{3+}) is above the values reported for $FeNbO_4$ [47]. The evolution of the parameters extracted from the EPR data, *g*, H_{res} and ΔH_{pp} as a function of the Ni concentration at 77 and 300K are presented in Fig. 8(c–e).

3.7. Hydrogen evolution reaction

The electrocatalytic performance of the $Fe_{1-x}Ni_xNbO_4$ ($0.00 \leq x \leq 0.20$) samples in alkaline medium was evaluated using different electrochemical techniques in order to investigate the role of dopant Ni^{2+} incorporation in the HER. The LSV curves in Fig. 9(a) show a progressive decrease in the overpotential required to reach 10 mA cm^{-2} as the Ni content increases. The $FeNbO_4$ sample exhibits an overpotential of 684 mV, whereas $Fe_{0.90}Ni_{0.10}NbO_4$ and $Fe_{0.80}Ni_{0.20}NbO_4$ display significantly lower values of 647 mV and 617 mV, respectively. The 67 mV

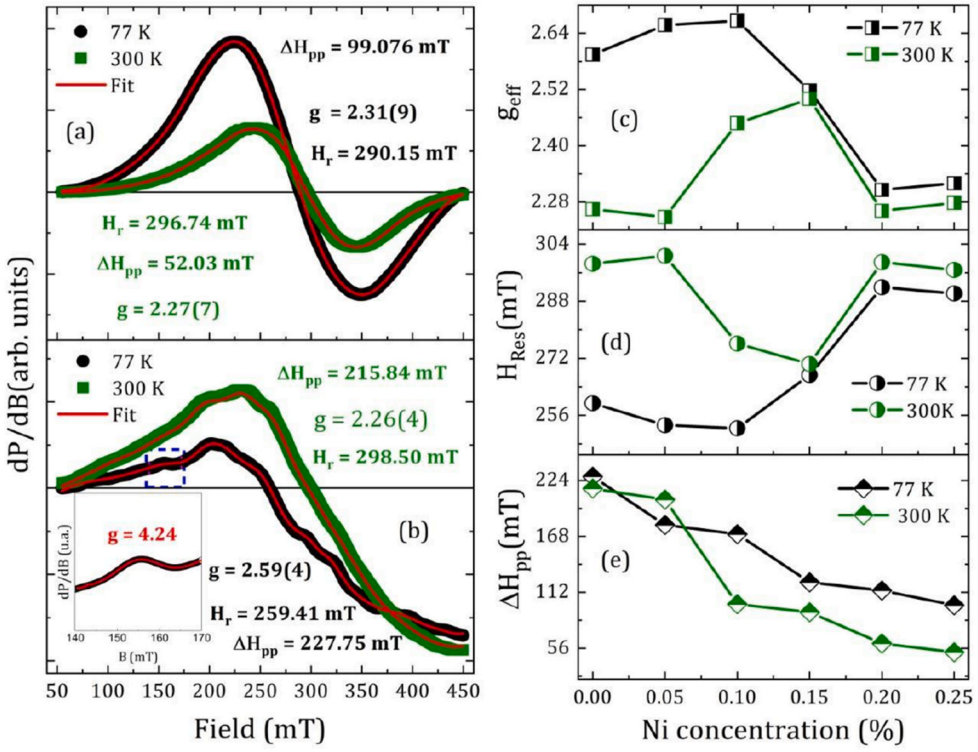

Fig. 8. EPR spectra for $Fe_{1-x}Ni_xNbO_4$ measured at room temperature (300 K) and 77 K: (a) $x = 0.25$ and (b) $x = 0.0$ (c) *g*-factor, (d) resonant a-field (H_{res}) and (e) peak-to-peak linewidth (ΔH_{pp}) as a function of Ni concentration, measured at 300 K and 77 K.

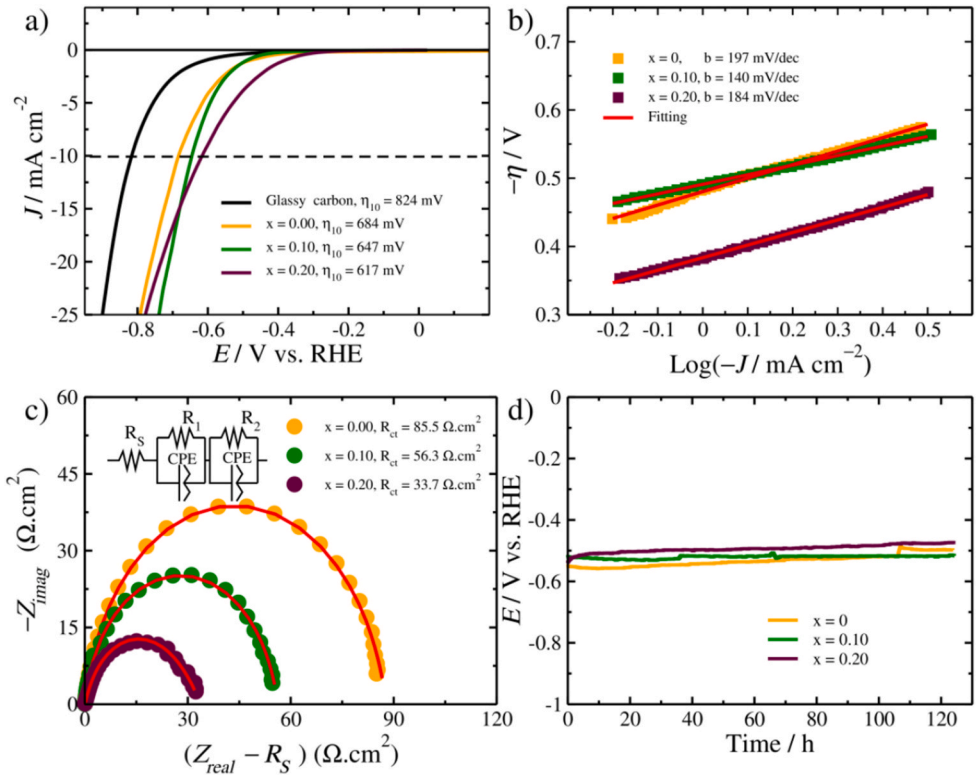

Fig. 9. Electrochemical test: (a) The polarization curves for HER electrocatalyst. (b) Tafel slope with linear fitting. (c) Nyquist plots from EIS. (d) Stability tests in continuous operation at 10 mA cm^{-2} for 120 h for sample $x = 0.0$, 0.10 and 0.20.

reduction between the undoped sample and the $x = 0.20$ composition clearly indicates that Ni^{2+} acts as an efficient dopant, enhancing the electrocatalytic activity of $FeNbO_4$. This trend is consistent with other Ni-doped oxide-based systems reported in the literature, where Ni sites exhibit more favorable hydrogen adsorption energies (low Gibbs free energy of adsorption of hydrogen (ΔG_{H^*})) and promote fast charge

transport by modulating the electronic environment of the active sites [48–50]. Furthermore, to elucidate the reaction mechanism, Tafel plots were constructed from the LSV curves, as shown in Fig. 9(b). The fitting of the polarization data to the Tafel equation [51,52] yielded slopes of 197 mV dec^{-1} for $FeNbO_4$, 140 mV dec^{-1} for $Fe_{0.90}Ni_{0.10}NbO_4$, and 184 mV dec^{-1} for $Fe_{0.80}Ni_{0.20}NbO_4$. According to the theoretical mechanisms of HER in alkaline media, Tafel slopes exceeding 120 mV dec^{-1} are characteristic of a mechanism in which the Volmer step (electrochemical water dissociation, $H_2O + e^- \rightarrow H^*$) acts as the rate-determining step [52]. When this criterion is applied to our results, all $Fe_{1-x}Ni_xNbO_4$ compositions clearly fall within the Volmer–Heyrovsky regime, with the Volmer step acting as the rate-determining step. The Tafel slopes and overpotential values obtained are in good agreement with those reported for other transition-metal-based electrocatalysts, as summarized in Table 4.

Electrochemical impedance spectroscopy (EIS) was used to evaluate the charge-transfer properties of the $Fe_{1-x}Ni_xNbO_4$ samples. The Nyquist plots shown in Fig. 9(c) reveal a systematic reduction in charge-transfer resistance (R_{ct}) with increasing Ni^{2+} concentration. While $FeNbO_4$ exhibits R_{ct} = 85.5 Ω cm^2, the $Fe_{0.90}Ni_{0.10}NbO_4$ and $Fe_{0.80}Ni_{0.20}NbO_4$ samples show lower values of 56.3 Ω cm^2 and 33.7 Ω cm^2, respectively. These results indicate that Ni^{2+} significantly improves the electronic conductivity of the oxide lattice and facilitates electron transport through Ni–O–Fe linkages, a behavior consistent with electronic-modulation effects reported for Ni/Fe systems [1,53]. The reduction in Rct accompanies the decrease in Tafel slope and overpotential, reinforcing the structural evidence that Ni doping modifies $FeNbO_4$ in a manner favorable for HER. In this context, the HER performance observed in this work should be interpreted within the class of non-noble metal oxide electrocatalysts. Although the overpotential values remain higher than those of benchmark noble metal catalysts such as Pt/C, Ni^{2+} incorporation clearly enhances the electrocatalytic activity of $FeNbO_4$ compared to the undoped sample, as summarized in Table 4. Finally, the operational durability of all studied samples, namely $FeNbO_4$, $Fe_{0.90}Ni_{0.10}NbO_4$, and $Fe_{0.80}Ni_{0.20}NbO_4$, was investigated under constant electrolysis at 10 mA cm^{-2} for 120 h (Fig. 9(d)). All samples exhibited stable electrochemical behavior, maintaining nearly constant potentials throughout the experiment. The small oscillations observed are attributed to the periodic accumulation and detachment of H_2 bubbles from the electrode surface, a behavior widely reported in the literature [54,55]. Overall, the stability tests confirm that the studied materials maintain good electrochemical stability under alkaline HER conditions, which is an important factor in evaluating their practical applicability.

4. Conclusions

The gradual incorporation of Ni into the $FeNbO_4$ structure induces significant modifications in its structural, vibrational, optical, and magnetic properties. The substitution of Fe^{3+} by Ni^{2+} introduces local lattice distortions, leading to a systematic increase in the lattice parameters, as evidenced by Rietveld refinement of the XRD patterns and Raman spectroscopy analyses. Moreover, Ni doping promotes a magnetic phase transition from antiferromagnetic to ferrimagnetic ordering. This transition can be associated with a magnetic symmetry breaking due to the difference in magnetic moment between the Fe^{3+} ($3\,d^5$, $S = 5/2$) and Ni^{2+} ($3\,d^8$, $S = 1$) ions. Thus, the exchange interactions between Ni^{2+} and Fe^{3+} ions, mediated by oxygen (Ni^{2+}-O-Fe^{3+}), and the contribution of defects such as oxygen vacancies, are the main responsible for the observed FiM order. Electrochemical measurements demonstrated promising activity in the hydrogen evolution reaction (HER), with an overpotential of approximately 617 mV at a current density of 10 $mAcm^{-2}$ and a Tafel slope of 184 mV/decade for the composition $x = 0.20$. Furthermore, a negligible loss of overpotential was observed after 120 consecutive hours of hydrogen evolution. These results suggest that Ni-doped $FeNbO_4$ possesses considerable potential for applications in sustainable hydrogen production.

CRediT authorship contribution statement

Diego S. Evaristo: Writing – review & editing, Methodology, Formal analysis, Data curation, Conceptualization. **Raí F. Jucá:** Investigation, Formal analysis, Data curation. **Francisco G.S. Oliveira:** Writing – review & editing, Methodology, Formal analysis, Data curation. **Gilberto D. Saraiva:** Writing – review & editing, Supervision, Project administration. **João M. Soares:** Writing – review & editing, Validation. **Teresa M. Barreto:** Writing – review & editing, Visualization, Validation. **Pedro Tavares:** Writing – review & editing, Visualization, Validation. **Benilde F.O. Costa:** Writing – review & editing, Visualization, Validation, Supervision. **José A. Paixão:** Writing – review & editing, Visualization, Validation, Data curation. **Ana C. Silva:** Data curation, Writing – review & editing. **Nilson S. Ferreira:** Writing – review & editing, Validation, Supervision. **Marcelo A. Macedo:** Writing – review & editing, Validation, Supervision. **Antônio J.R. Castro:** Validation, Supervision, Project administration.

Declaration of competing interest

The authors declare that they have no known competing financial interests or personal relationships that could have appeared to influence

Table 4
Comparison electrocatalytic activity for HER of electrocatalyst $Fe_{(1-x)}Ni_xNbO_4$ with several recently reported electrocatalysts.

Electrocatalysts	b mV dec^{-1}	η *mV at*10 mA cm^{-2}	electrolyte	substrate	catalyst loadingmgcm^{-2}	Reference
x = 0.00	***197***	***684***	**1 M NaOH**	GCE*	***0.027***	***This work***
x = 0.10	***140***	***647***	**1M NaOH**	GCE*	***0.027***	***This work***
x = 0.20	***184***	***617***	**1M NaOH**	GCE*	***0.027***	***This work***
WO_3/NC	*137*	*745*	1 M KOH	GCE*	0.001	[56]
$SrLaFeO_4$	*258*	*691*	1 M KOH	GCE*	0.001	[8]
$SrLaCo_{0.5}Fe_{0.5}O_4$	*216*	*622*	1 M KOH	GCE*	0.001	[8]
MoS_2/C-600	*260*	*689*	0.5 M H_2SO_4	GCE*	0.002	[5]
Sr_3MnO_6	*240*	*590*	1 M KOH	GCE*		[4]
Fe-600C@BMC	*222*	*550*	0.5 M H2SO4	GCE*		[57]
Ni_3Fe@BC-600	*140*	*500*	1 M KOH	GCE*	0.0034	[58]
Sr_3FeMnO_6	*214*	*450*	1 M KOH	GCE*		[4]
$SrNb_{0.1}Co_{0.7}Fe_{0.2}O_{3-\delta}$	*171*	*361*	1 M KOH	GCE*	0.002	[9]
$FeNbO_4$@C	*110*	*283*	1.0 M KOH	GCE*		[7]
$FeNbO_4$	*160*	*373*	1.0 M KOH	GCE*		[7]
MoS2	*114*	*175*	1.0 M KOH	Ni foam	0.001	[59]
$Fe_{0.80}Co_{0.20}NbO_4$	*156*	*620*	**1M NaOH**	GCE*	***0.027***	[2]
MoS2/NiO	*232*	*530*	1 M NaOH	GCE*		[60]
MoS2/NiO/MWCNT	*220*	*510*	1 M NaOH	GCE*		[60]

the work reported in this paper.

Acknowledgements

Diego S. Evaristo and Antônio J. R. Castro thanks FUNCAP/Edital 09/2023 (Grants# FPD-0213-00238.01.00/23). Antônio J. R. Castro acknowledges the support from the MCTI/CNPQ PQ-09/2022 (Grants# 310440/2022-0). Gilberto D. Saraiva, Ph.D., acknowledges the support from the FUNCAP/Edital 06/2023 (Grants# UNI-0210-00410.01.00/23), FUNCAP/Edital 09/2023 (Grants# FPD-0213-00204.01.00/23) and the MCTI/CNPQ PQ – 09/2023 (Grants#308449/2023-1). Francisco G. S. Oliveira, acknowledges FUNCAP scholarship (EDITAL 09/2023 FUNCAP – PÓS-DOUTORADO). The authors would like to thank the Laborátorio de Pesquisa em Corrosão (LPC) at the Federal University of Ceará for the infrastructure provided, which was essential for the completion of this study. Raí F. Jucá, Ph.D., acknowledges the financial support of the National Council for Scientific and Technological Development (CNPq), Brazil, under Call No. 49/2024-PDJ (N° 151882/2025-8). FCT-NOVA acknowledged the Portuguese Science Foundation through the programme UID/00068/2025 (https://doi.org/10.54499/UID/00068/2025). FisUC acknowledges FCT through the programme UID/04564/2025. The authors acknowledge Dr Nenad Bundaleski for recording the XPS spectra.

Appendix A. Supplementary data

Supplementary data to this article can be found online at https://doi.org/10.1016/j.jpcs.2026.113756.

Data availability

Data will be made available on request.

References

[1] H. Xun, T. Liu, J. Zhang, C. Yan, Y. Ju, L. Shi, Q. Che, D. Zhao, M. Zuo, Fabrication of self-supported bulk (Ni_xFe_y)–B@Cu metallic catalysts for hydrogen evolution reaction, Mater. Sci. Eng. B 318 (2025) 118294.

[2] R.F. Jucá, D.S. Evaristo, F.G. Oliveira, L.P. Santos, G.D. Saraiva, A.J. Castro, N. S. Ferreira, L.F. Lobato, J.M. Soares, A.L.B. Brito, R. Fausto, M.A. Macêdo, B. F. Costa, Co-doped $FeNbO_4$: simple synthesis, DFT calculations and electrocatalytic performance for the hydrogen evolution reaction in alkaline medium, J. Phys. Chem. Solid. 202 (2025) 112649.

[3] H.B. Silva, D.S. Luz, F.G.S. Oliveira, R.F. Jucá, D.S. Evaristo, J.M. Soares, A.J. R. d. Castro, V.O. Neto, M.A. Macêdo, G.D. Saraiva, Synthesis and electrocatalytic evaluation of magnetic FeM (M = Co, Ni, Cu and Mn) alloys for water splitting applications, Mater. Chem. Phys. 348 (2026) 131693.

[4] S.B. Karki, R.K. Hona, F. Ramezanipour, $Sr_3Mn_2O_6$ and Sr_3FeMnO_6 for oxygen and hydrogen evolution electrocatalysis, J. Solid State Electrochem. 26 (2022) 1303–1311.

[5] J.-D. Yi, T.-T. Liu, Y.-B. Huang, R. Cao, Solid-state synthesis of MoS_2 nanorod from molybdenum-organic framework for efficient hydrogen evolution reaction, Sci. China Mater. 62 (2019) 965–972.

[6] Y. Abghoui, E. Skúlason, Hydrogen evolution reaction catalyzed by transition-metal nitrides, J. Phys. Chem. C 121 (2017) 24036–24045.

[7] H. Fu, Y. Bai, Y. Lian, Y. Hu, J. Zhao, H. Zhang, Oxygen-deficient $FeNbO_{4-x}$ In-Situ growth in honey-derived N-Doping porous carbon for overall water splitting, ChemSusChem 17 (2024) e202400162.

[8] M.S. Alom, F. Ramezanipour, Layered oxides $SrLaFe_{1-x}Co_xO_{4-\delta}$ (x=0–1) as bifunctional electrocatalysts for water-splitting, ChemCatChem 13 (2021) 3510–3516.

[9] Y. Zhu, W. Zhou, Y. Zhong, Y. Bu, X. Chen, Q. Zhong, M. Liu e Z. Shao, A perovskite nanorod as bifunctional electrocatalyst for overall water splitting, Adv. Energy Mater. 7 (2017) 1602122.

[10] W. Harrison, A. Cheetham, Structural and magnetic properties of $FeNbO_4$ - II, Mater. Res. Bull. 24 (1989) 523–527.

[11] X. Wang, D. Santos-Carballal, N.H.d. Leew, Density functional theory study of Monoclinic $FeNbO_4$: Bulk properties and water dissociation at the (010), (011), (110), and (11) surfaces, J. Phys. Chem. C 125 (2021) 27566–27577.

[12] C. Liu, R. Chen, X. Yue, Y. Liu, M. Shi, H. Zhua, C. Dong, Y. Liu, Y. Han, J. Wang, Z. He, Crystal growth, magnetic property and phase transition of the zigzag-chain antiferromagnet $FeNbO_4$, J. Magn. Magn Mater. 464 (2018) 108–111.

[13] R.S. Roth, J.L. Waring, Ixiolite and other polymorphic types of $FeNbO_4$, Am. Mineral. 49 (1964) 242–246.

[14] N. Lakshminarasimhan, A.N. Kumar, S.S. Chandrasekaran, P. Murugana, Structure-magnetic property relations in $FeNbO_4$ polymorphs: a spin glass perspective, Prog. Solid State Chem. 54 (2019) 20–30.

[15] R. Theissmann, H. Ehrenberg, H. Weitzel, H. Fuess, Domain structure and lattice strains in $FeNbO_4$, Solid State Sci. 7 (2005), 791-79.

[16] S.H. Ahmed, M. Bakiro, A. Alzamly, Effect of pH and surfactant on band gap properties of monoclinic $FeNbO_4$ prepared via different routes, Nano-Struct. Nano-Objects 20 (2019) 100400.

[17] C. Balamurugan, A. Maheswari, D. Lee, A. Subramania, Selective ethanol gas sensing behavior of mesoporous n-type semiconducting $FeNbO_4$ nanopowder obtained by niobium–citrate process, Curr. Appl. Phys. 14 (2014) 439–446.

[18] M. He, D. Li, Y. Liu, T. Li, F. Li, J. Fernandez-Catala, W. Cao, One-pot hydrothermal synthesis of $FeNbO_4$ microspheres for effective sonocatalysis, New J. Chem. 48 (2024) 6704–6713.

[19] C. Iwasaki, Y. Yoshiyama, S. Hosokawa, N. Nagata, A. Dejima, K. Onishi, R. Maeda, S. Naniwa, S. Iguchi, H. Asakura, K. Teramura, T. Tanaka, Oxygen storage property and catalytic performance of Ti-Doped $FeNbO_4$, J. Phys. Chem. C 128 (2024) 9884–9893.

[20] I.-S. Cho, S. Lee, J.H. Noh, G.K. Choi, H.S. Jung, D.W. Kim, K.S. Hong, Visible-light-induced photocatalytic activity in $FeNbO_4$ nanoparticles, J. Phys. Chem. C 112 (2008) 18393–18398.

[21] B.M.F. Jones, D. Maruthamanib, V. Muthuraj, Construction of novel n-type semiconductor anchor on 2D honey comb like $FeNbO_4$/RGO for visible light drive photocatalytic degradation of norfloxacin, J. Photochem. Photobiol. Chem. 400 (2020) 112712.

[22] S. Devesa, M. Graça, F. Henry, L. Costa, Dielectric properties of $FeNbO_4$ ceramics prepared by the sol-gel method, Solid State Sci. 61 (2016) 44–50.

[23] T. Wang, S. Shi, F. Kong, G. Yang, B. Qian, F. Yin, The role of stable interface in nano-sized $FeNbO_4$ as anode electrode for lithium-ion batteries, Electrochim. Acta 203 (2016) 206–212.

[24] T.S.D. Kumari, R.V. Gandhi, G. Rahul, G. Kamalanathan, T.P. Kumar, D. Jeyakumar, N. Lakshminarasimhan, Electrochemical lithium insertion behavior of $FeNbO_4$: structural relations and in situ conversion into $FeNb_2O_6$ during carbon coating, Mater. Chem. Phys. 145 (2014) 425–433.

[25] X. Liu, D. Xie, J.T. Irvine, J. Ni, C. Ni, An $FeNbO_4$-based oxide anode for a solid oxide fuel cell (SOFC), Electrochim. Acta 335 (2020) 135692.

[26] H. Ehrenberg, G. Wltschek, R. Theissmann, H. Weitzel, H. Fuess, F. Trouw, The magnetic structure of $FeNbO_4$, J. Magn. Magn Mater. 218 (2000) 261–265.

[27] D.S. Evaristo, R.F. Jucá, J.M. Soares, R.B. Silva, G.D. Saraiva, R.S. Matos, N. S. Ferreira, M. Salerno, M.A. Macêdo, Antiferromagnet–Ferromagnet transition in $Fe_{1-x}Cu_xNbO_4$, Materials 15 (2022) 7424.

[28] B.H. Toby, EXPGUI, a graphical user interface for GSAS, J. Appl. Crystallogr. 34 (2001) 210–213.

[29] Y. Liu, H. Wang, G. Chen, Y.D. Zhou, B.Y. Gu, B.Q. Hu, Analysis of Raman spectra of ZnWO4 single crystals, J. Appl. Phys. 64 (1988) 4651–4653.

[30] J. Ruiz-Fuertes, D. Errandonea, S. López-Moreno, J. González, O. Gomis, R. Vilaplana, F.J. Manjón, P.A. Muñoz, Rodríguez-Hernández, A. Friedrich, I. A. Tupitsyna, L.L. Nagornaya, High-pressure Raman spectroscopy and lattice-dynamics calculations on scintillating $MgWO_4$: comparison with isomorphic compounds, Phys. Rev. B 83 (2011) 214112.

[31] K. Ishii, N. Morita, H. Nakayama, S. Tsunekawa, T. Fukuda, Raman Spectra of $LaNbO_4$ in the ferroelastic phase and the relaxation after the state shift, Phys. Stat. Sol. A 112 (1989) 207.

[32] T.T. Basiev, A.Y. Karasik, A.A. Sobol, D.S. Chunaev, V.E. Shukshin, Spontaneous and stimulated Raman scattering in $ZnWO_4$ crystals, Quant. Electron. 41 (2011) 370.

[33] Q. Zhang, L. Xu, X. Tang, F. Huang, X. Wu, Y. Li, Y. Jing, Z.-K. Hand, H. Su, Electronic structure, Raman spectra, and microwave dielectric properties of Co-substituted $ZnWO_4$ ceramics, J. Alloys Compd. 874 (2021) 159928.

[34] A. Rajan, M. Sharma, N.K. Sahu, Assessing magnetic and inductive thermal properties of various surfactants functionalised Fe_3O_4 nanoparticles for hyperthermia, Sci. Rep. 10 (2020) 15045.

[35] Raí F. Jucá, Diego S. Evaristo, Bruno J.C. Vieira, João C. Waerenborgh, Ana C. Silva, I. Orue, Fernando Plazaola, João M. Soares, Gilberto D. Saraiva, João G. de Oliveira Neto, Nilson S. Ferreira, Marcelo M. Macêdo, José A. Paixão, Benilde F. O. Costa, Defect-engineered $Fe_{0.9}Co_{0.1}NbO_{4-\delta}$ ceramics: oxygen vacancy-mediated magnetic behavior and phase stability, Ceramics Internacional xx (2026), https://doi.org/10.1016/j.ceramint.2026.02.223 xxxx-xxxx.

[36] H. Abdel-Samad, P.R. Watson, An XPS study of the adsorption of chromate on goethite (α-FeOOH), Appl. Surf. Sci. 108 (1997) 371–377.

[37] N. Özer, M.D. Rubin, C.M. Lampert, Optical and electrochemical characteristics of niobium oxide films prepared by sol-gel process and magnetron sputtering A comparison, Sol. Energy Mater. Sol. Cell. 40 (1996) 285–296.

[38] T. Zheng, F. Wu, H. Fu, L. Zeng, C. Shang, L. Zhu, Z. Guo, Rational design of Pt- Pd-Ni trimetallic nanocatalysts for roomtemperature benzaldehyde and styrene hydrogenation, Chem. Asian J. 16 (2021) 1–10.

[39] W. Zhang, H. Shen, M. Yin, L. Lu, B. Xu, D. Li, Heterostructure silicon solar cells with enhanced power conversion efficiency based on Six/Ni^{3+} self-doped NiOx passivating contact, ACS Omega 7 (2022) 16494–16501.

[40] Y. Chang, L. Gao, Y. Xie, B. You, Y. Liu, R. Xiong, J. Wang, C. Lu, J.-M. Liu, Antiferromagnetic to Ferrimagnetic phase transition and possible phase coexistence in polar Magnets $(Fe_{1-x}Mn_x)_2Mo_3O_8$ ($0 \leq x \leq 1$), ACS Appl. Mater. Interfaces 15 (2023) 22204–22211.

[41] Y. Chang, B. You, Y. Xie, Y. Liu, R. Xiong, J.-M.L. Chengliang Lu, Tuning magnetic properties of polar magnets $(Mn_{1-x}Co_x)_2Mo_3O_8$ ($0 < x < 1$) with interacted magnetic sublattices, Appl. Phys. Lett. 123 (2023) 102402.

[42] J. López-Sánchez, A.d. Campo, S. Román-Sánchez, Ó.R.d. l. Fuente, N. Carmona, A. Serrano, Large two-magnon raman hysteresis observed in a magnetically uncompensated hematite coating across the morin transition, Coatings 12 (2022) 540.
[43] S. Mugiraneza, A.M. Hallas, Tutorial: a beginner's guide to interpreting magnetic susceptibility data with the Curie-Weiss law, Commun. Phys. 5 (2022) 95.
[44] D.S. Evaristo, R.S.S. Jr, R.F. Jucá, C. Santos, G.D. Saraiva, J. Gainza, J.E. Rodrigues, E. Céspedes, J.L. Martínez, J.A. Alonso, I.F. Vasconcelos, F.G.S. Oliveira, N. S. Ferreira, A.J.R. Castro, E.C. Passamani, M.A. Macêdo, Magnetic phase transition in the quasi-one-dimensional spin chain system $Fe_{0.75}Cu_{0.25}NbO_4$, ACS Omega 10 (2025) 62645–62656.
[45] K.V.P.M. Shafi, Y. Koltypin, A. Gedanken, R. Prozorov, J. Balogh, J. Lendvai, I. Felner, Sonochemical preparation of nanosized amorphous $NiFe_2O_4$ particles, J. Phys. Chem. B 101 (1997) 6409–6414.
[46] G. Alvarez, R. Font, J. Portelles, O. Raymond, R. Zamorano, Paramagnetic resonance and non-resonant microwave absorption in iron niobate, Solid State Sci. 11 (2009) 881–884.
[47] Q. Chen, H. Zhang, Y. Feng, B. Miao, High polarizability enhanced EPR, optical linear & nonlinear and electric conductivity: role of $NiFe_2O_4$ nanocrystals in transparent tellurite glass-ceramics, J. Alloys Compd. 930 (2023) 167394.
[48] C. Hu, J. Hong, J. Huang, W. Chen, C.U. Segre, K. Suenaga, W. Zhao, F. Huang, J. Wang, Surface decoration accelerates the hydrogen evolution kinetics of a perovskite oxide in alkaline solution, Energy Environ. Sci. 13 (2020) 4249.
[49] W. Liu, P. Geng, S. Li, W. Liu, D. Fan, H. Lu, Z. Lu, Y. Liu, Tuning electronic configuration of WP_2 nanosheet arrays via nickel doping for high-efficiency hydrogen evolution reaction, J. Energy Chem. 55 (2021) 17–24.
[50] M. Liu, H. Li, S. Liu, L. Wang, L. Xie, Z. Zhuang, C. Sun, J. Wang, M. Tang, S. Sun, S. Liu, Q. Zhao, Tailoring activation sites of metastable distorted 1T′-phase MoS_2 by Ni doping for enhanced hydrogen evolution, Nano Res. 15 (2022) 5946–5952.
[51] J. Wang, F. Xu, H. Jin, Y. Chen, Y. Wang, Non-noble metal-based carbon composites in hydrogen evolution reaction: fundamentals to applications, Adv. Mater. 29 (2017) 605838.
[52] J. Theerthagiri, S.J. Lee, A.P. Murthy, J. Madhavan, Fundamental aspects and recent advances in transition metal nitrides as electrocatalysts for hydrogen evolution reaction: a review, Curr. Opin. Solid State Mater. Sci. 24 (2020) 100805.
[53] L. Trotochaud, S.L. Young, J.K. Ranney, S.W. Boettcher, Nickel−Iron oxyhydroxide oxygen-evolution electrocatalysts: the role of intentional and incidental iron incorporation, J. Am. Chem. Soc. 136 (2014) 6744–6753.
[54] B.S. Singu, R.K. Chitumalla, D. Mandal, Y. Kim, G.H. Kim, H.T. Chung, J. Jang, H. Kim, Development of metal-organic framework-derived NiMo-MoO_{3-x} porous nanorod for efficient electrocatalytic hydrogen evolution reactions, Appl. Catal. B Environ. 328 (2023) 122421.
[55] S. Park, A. Bashkatov, J.J.J. Eggebeen, S. Lee, D. Lohse, D. Krug, M.T.M. Koper, Combined effects of electrode morphology and electrolyte composition on single H_2 gas bubble detachment during hydrogen evolution reaction, Nanoscale 17 (2015) 10020.
[56] T. Feng, Z. Cui, P. Guo, X. Wang, J. Li, X. Liu, W. Wang, Z. Li, Fabrication of Ru/WO_3-W_2N/N-doped carbon sheets for hydrogen evolution reaction, J. Colloid Interface Sci. 636 (2023) 618–626.
[57] M.A. Ahsan, A.R.P. Santiago, A. Rodriguez, V. Maturano-Rojas, B. Alvarado-Tenorio, R. Bernal, J.C. Noveron, Biomass-derived ultrathin carbon-shell coated iron nanoparticles as high-performance tri-functional HER, ORR and Fenton-like catalysts, J. Clean. Prod. 275 (2020) 124141.
[58] Y.B. Adegbemiga, N. Ullah, M. Xie, S. Hussain, C.J. Oluigbo, W. Yaseen, A. J. Kumar, Y. Xu, J. Xie, Ni_3Fe nanoparticles enclosed by B-doped carbon for efficient bifunctional performances of oxygen and hydrogen evolution reactions, J. Alloys Compd. 835 (2020) 155267.
[59] R.K. Mishra, G.J. Choi, J.W. Ryu, H.J. Jeon, S.H. Jin, R. Bhardwaj, S. Arya, J. S. Gwag, Exploring the electrocatalytic properties of binder-free RGO/MoS_2 heterostructure for hydrogen evolution reaction, Mater. Sci. Eng. B 318 (2025) 118292.
[60] B. Lai, S.C. Singh, J. Bindra, C. Saraj, A. Shukla, T. Yadav, W. Wu, S. McGill, N. Dalal, A. Srivastava, C. Guo, Hydrogen evolution reaction from bare and surface-functionalized few-layered MoS_2 nanosheets in acidic and alkaline electrolytes, Mater. Today Chem. 14 (2019) 100207.